

Pi-GS: Sparse-View Gaussian Splatting with Dense π^3 Initialization

Manuel Hofer Markus Steinberger Thomas Köhler
 Graz University of Technology
 Austria

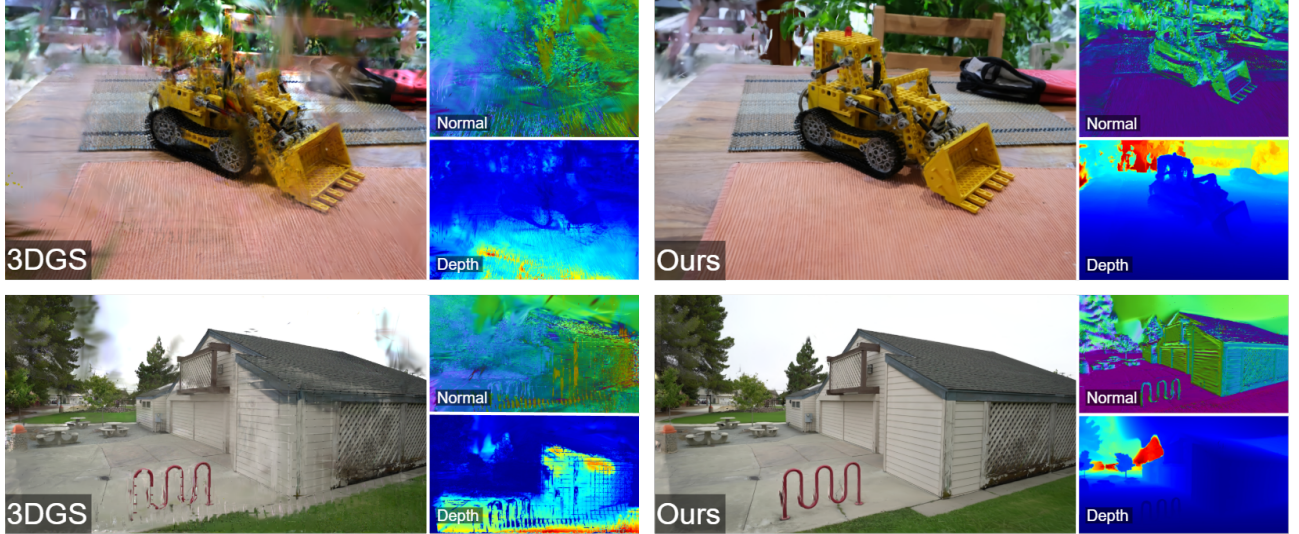


Figure 1. 3DGS exhibits floaters and view inconsistencies under sparse-view constraints. These artifacts are mostly caused by depth ambiguities and poor Gaussian alignment with the underlying geometry, as shown in the depth and normal maps. By incorporating depth supervision, normal supervision, and additional pseudo views, our method significantly reduces these artifacts and produces more view-consistent novel views with improved Gaussian alignment under sparse-view constraints.

Abstract

Novel view synthesis has evolved rapidly, advancing from Neural Radiance Fields to 3D Gaussian Splatting (3DGS), which offers real-time rendering and rapid training without compromising visual fidelity. However, 3DGS relies heavily on accurate camera poses and high-quality point cloud initialization, which are difficult to obtain in sparse-view scenarios. While traditional Structure from Motion (SfM) pipelines often fail in these settings, existing learning-based point estimation alternatives typically require reliable reference views and remain sensitive to pose or depth errors. In this work, we propose a robust method utilizing π^3 , a reference-free point cloud estimation network. We integrate dense initialization from π^3 with a regularization scheme designed to mitigate geometric inaccuracies. Specifically, we employ uncertainty-guided depth supervision, normal consistency loss, and depth warping. Experimental results demonstrate that our approach achieves state-of-the-art performance on the Tanks and Temples, LLFF, DTU, and MipNeRF360 datasets.

1. Introduction

3D scene reconstruction and novel view synthesis (NVS) are rapidly advancing, with many applications across different domains [32]. These methods can be applied in fields such as Virtual Reality (VR) for creating immersive worlds, cinematography to create visually appealing assets efficiently, or robot vision to help robots understand their physical environment [23]. The foundation of 3D scene reconstruction was laid by traditional Structure from Motion pipelines. More recently, significant advances in NVS were achieved by representing the scene as Neural Radiance Fields (NeRF) [16]. These methods achieve state-of-the-art results but suffer from slow training speeds and are unsuitable for real-time rendering due to high latency. Newer methods such as 3D Gaussian Splatting (3DGS) [11] enable high-quality NVS even for real-time rendering. Additionally, training speed is significantly reduced.

A major limitation of these novel view synthesis methods is the need for dense views, which often is not feasible for real-world applications. In sparse-view settings, these methods tend to struggle with bad initialization,

depth ambiguities and overfitting to training views. To improve the performance in these settings and counteract the depth ambiguities, certain priors are introduced to better generalize and escape minima throughout the optimization process. Methods such as *DNGaussian* [14] and *Few-shot Novel View Synthesis using Depth* [13] leverage monocular depth estimators to regularize the model with the help of the inferred depth. The depth regularization helps significantly to improve the depth ambiguities and increase the generalization capability of the models. A challenge for these models is correct depth scaling, proper point initialization, and accurate camera poses. The initial points and camera poses are traditionally generated using Structure from Motion (SfM) pipelines. However, these pipelines often struggle with sparse input views and limited overlap between views. Recent advancements for sparse-view settings were achieved by leveraging dense initialization with the help of point cloud estimation networks [27, 28, 31]. They replace the traditional SfM pipeline with models such as *MAS3R* [7] or *DUS3R* [24] for the point cloud estimation and camera pose estimation. The resulting models achieve high-fidelity results but require good initial reference views for accurate predictions. In addition, a time-consuming iterative camera alignment process is required, which can take several minutes. Inaccurate camera poses may further reduce reconstruction quality.

We make the following contributions:

- We discuss a method for leveraging a Permutation-Equivariant point cloud estimation network for dense initialization without relying on traditional SfM.
- We introduce confidence aware pearson depth loss, to counteract uncertain depth estimations.
- We explore the use of PGSR in sparse-view settings for improved geometry alignment and reduced overfitting.

Our method achieves state-of-the-art results in sparse-view settings and significantly improves Gaussian surface alignment, while reducing floaters. Our code is publicly available at <https://github.com/Mango0000/Pi-GS>.

2. Related Work

This section reviews prior work on 3D reconstruction, covering classical geometry-based pipelines, neural radiance fields, and Gaussian splatting approaches, with a focus on sparse-view and pose-free scenarios.

2.1. Traditional 3D Reconstruction

Classical 3D reconstruction pipelines typically rely on Structure-from-Motion (SfM) to achieve camera pose estimation and to generate a point cloud from a given set of images taken from various viewpoints. Afterward, Multi-View Stereo (MVS) and surface reconstruction techniques such as Poisson reconstruction are used [10, 20, 34]. These methods perform well in textured and opaque scenes but struggle with transparent materials and sparse or low-overlap views. Moreover, they are highly sensitive

to SfM failures, which can lead to unstable surface reconstruction.

2.2. Neural Radiance Fields

Neural Radiance Fields (NeRF) [16] represent scenes by continuous volumetric functions. This makes them capable of producing photorealistic novel views and handling view-dependent effects more accurately. However, a downside is that NeRFs are quite demanding in terms of computation. As a result, we see more efficient variants like *Instant-NGP* [17], *PlenOctree* [30] and *Efficient-NeRF* [9] that drastically shorten the training and rendering time by incorporating optimized data structures and improving the architecture.

2.3. 3D Gaussian Splatting

3D Gaussian Splatting (3DGS) [11] has emerged as a new method that improves on training and rendering speed by replacing the implicit radiance field of NeRF-based methods with an explicit representation. Its core idea is to use 3D Gaussians both for optimization and for rendering via rasterization, therefore achieving real-time rendering without losing either fine details or transparency. Advanced 3DGS methods, such as *PGSR: Planar-based Gaussian Splatting for Efficient and High-Fidelity Surface Reconstruction* (PGSR) [4], improve Gaussian surface alignment with the help of planar Gaussians and multi-view consistency losses. However, these methods generally rely on SfM for initialization and are optimized for dense and overlapping views.

2.4. Sparse-View Gaussian Splatting

Reconstruction from sparse views remains a major challenge for 3DGS. Several augmentations exist that address sparse-view reconstruction by introducing additional constraints and regularization terms. Depth-based supervision is explored in *Depth-Regularized 3D Gaussian Splatting* [6], *Few-shot NVS with Depth-Aware 3D Gaussian Splatting* [13], and *DNGaussian* [14]. This type of supervision results in fast convergence and reduces depth ambiguities. Meanwhile, *DropGaussian* [18] and *DropoutGS* [29] deactivate Gaussians at random in order to counteract overfitting. There are also more advanced methods like *FSGS: Real-Time Few-Shot View Synthesis using Gaussian Splatting* [33] which introduces a pooling strategy and fine-tunes the splitting strategy to improve sparse view reconstruction across different datasets. While these methods achieve very robust results in sparse-view scenarios, they typically rely on accurate camera poses from SfM.

2.5. SfM-Free Methods

Methods such as *COLMAP-Free 3D Gaussian Splatting* [8] and *InstantSplat* [31], eliminate the need for SfM by jointly optimizing the 3D Gaussians as well as the camera poses and using depth estimations for point cloud initialization. These methods are able to handle sparse-view

situations more robustly and recover from inaccurate camera poses.

2.6. Diffusion-Based Priors

More recent works incorporate diffusion priors not only to stabilize the reconstruction, but also to generate additional views from the limited number of input views. *GenFusion* [26], *SparseGS* [28], *Gaussian Scenes* [19], and *Intern-GS* [27] are some of the methods where these advantages can also be observed. While these methods achieve impressive results, they often struggle with high-frequency textures and view inconsistencies due to depth ambiguities and inaccurate Gaussian alignment.

Our method differs fundamentally from diffusion-based and optimization-heavy approaches. Instead of synthesizing novel views using generative priors, we improve reconstruction quality through dense geometric initialization and strong generalizability across datasets. We leverage depth and normal supervision from estimated depth maps and explicitly model depth uncertainty through confidence-aware constraints, allowing deviations from noisy estimates. Camera poses and point representations are predicted by a feed-forward network, reducing reliance on iterative optimization and increasing robustness in sparse-view settings. Consequently, our approach focuses on geometric consistency and generalization without relying on view hallucination or diffusion-based priors.

3. Method

We begin by outlining preliminaries on Gaussian Splatting and planar depth rendering. Section 3.2 details modifications to PGSR for sparse settings, followed by our dense initialization strategy in Section 3.3. We then present our uncertainty-aware Pearson loss in Section 3.4 and artifact-free normal supervision in Section 3.5. Finally, Section 3.6 describes our depth warping approach for improving view consistency.

3.1. Preliminaries

Gaussian Splatting. *3D Gaussian Splatting* (3DGS) introduced by Kerbl et al. [11] achieves great novel view synthesis results with high efficiency by leveraging a Gaussian scene representation. Another improvement of this scene representation over NeRF is the real-time rendering speed, as well as much faster training times. Our approach also builds upon 3DGS. The scene representation is defined by a set of 3D Gaussians. Each Gaussian can be defined by a 3D covariance matrix $\Sigma \in \mathbb{R}^{3 \times 3}$ and the 3D center point $\mu \in \mathbb{R}^3$ in world space,

$$G(x) = e^{-\frac{1}{2}(x-\mu_i)^T \Sigma^{-1} (x-\mu_i)}. \quad (1)$$

To project this 3D Gaussian onto the 2D image plane for rendering, the covariance matrix Σ' in clip space is

defined as the following:

$$\Sigma' = JW\Sigma W^T J^T, \quad (2)$$

where J is the Jacobian of the affine approximation for this projection transformation and W is the view transformation matrix.

For the covariance matrix to be physically meaningful, it needs to be positive semi-definite. To ensure this throughout the training process, Σ is defined as the following:

$$\Sigma = RSS^T R^T, \quad (3)$$

where $S \in \mathbb{R}^{3 \times 3}$ is the scaling matrix, and $R \in \mathbb{R}^{3 \times 3}$ is the rotation matrix. This allows separate optimization of rotation and scaling and ensures that Σ is positive semi-definite. For increased memory efficiency, the rotation matrix is stored as a quaternion, and scaling as 3D vector.

Furthermore, for rendering the color C , we blend the colors of each Gaussian along the ray, as follows:

$$C = \sum_{i=1}^N T_i \alpha_i c_i, \quad (4)$$

where N is the number of Gaussians along a ray, c_i is the color of the i -th Gaussian represented by spherical harmonics (SH) to account for view dependent effects, α_i is the weighted opacity of the i -th Gaussian and T_i is the transmittance of the i -th Gaussian [11].

Transmittance T_i is defined as:

$$T_i = \prod_{j=1}^{i-1} (1 - \alpha_j). \quad (5)$$

By calculating the color for each ray from the camera, we can render an image. The training of this Gaussian representation is done by back propagation with the following loss function:

$$\mathcal{L} = (1 - \lambda) \mathcal{L}_1 + \lambda \mathcal{L}_{D-SSIM}, \quad (6)$$

where \mathcal{L}_1 is a simple l_1 loss between the rendered and ground-truth image and \mathcal{L}_{D-SSIM} is an image similarity measure between rendered and ground-truth image [2, 11]. 3DGS relies on camera poses and points obtained from structure from motion (SfM). However, in sparse-view settings, the resulting point cloud can be highly sparse, and the overlap between the images may be insufficient to extract reliable structures or accurate camera poses. This leads to a challenging starting point for 3DGS optimization.

Depth and Normal Rendering. We use *Planar-based Gaussian Splatting for Efficient and High-Fidelity Surface Reconstruction* [4] (PGSR) for normal and depth rendering. PGSR builds upon 3DGS, enabling the rendering and backpropagation of both the depth and normals. A naive

approach of computing the depth D of a pixel would be to use depth accumulation defined as:

$$D = \sum_{i=1}^N T_i \alpha_i z_i, \quad (7)$$

where T_i is the same as in Eq. (5), α_i is the weighted opacity of the i -th Gaussian and z_i is its distance from the camera [5]. PGSR on the other hand compresses the 3D Gaussians to get flat 2D planes, from which unbiased depth and normal maps can be rendered [4].

To get the 2D planes, PGSR flattens the 3D Gaussians by minimizing the minimum scale and therefore defining the scale loss \mathcal{L}_s as following:

$$\mathcal{L}_s = \|\min(s_1, s_2, s_3)\|_1, \quad (8)$$

where s_i is the i -th scale component of each Gaussian.

The direction of the minimum scale factor corresponds to the normal n_i . Therefore, the normals per ray, \mathcal{N} , can be rendered as following:

$$\mathcal{N} = \sum_{i=1}^N R_c^T n_i \alpha_i T_i, \quad (9)$$

where R_c is the rotation from the camera to the global world.

The distance d_i from the Gaussian plane to the camera center is defined as:

$$d_i = (R_c^T (\mu_i - T_c)) R_c^T n_i^T, \quad (10)$$

where T_c is the camera center in the world and μ_i is the center of the i -th Gaussian.

The distance D along a ray can now be defined as:

$$D = \sum_{i=1}^N d_i \alpha_i T_i. \quad (11)$$

PGSR extends 3DGS by introducing an Image Edge-Aware Single-View Loss \mathcal{L}_{svgeo} , which optimizes the Gaussian Scene with the Local Plane Assumption. This assumption states that two neighbouring pixels can be considered as an approximate local plane, but only if these pixels do not belong to an edge. The loss helps to improve the local depth and normal consistency. They also propose a Multi-View Geometric Consistency Loss, \mathcal{L}_{mvgeom} , which enhances geometric smoothness by projecting the depth and normals from one frame to another. Finally, they employ a Multi-View Photometric Consistency Loss, \mathcal{L}_{mvrgb} , which projects the grayscale image from one camera to another camera through depth warping [4].

3.2. PGSR Sparse-View

Default PGSR does not work well for the sparse-view setting out-of-the-box because of the multi-view observer



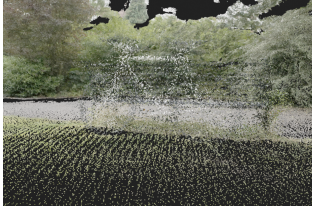
(a) Ballroom scene with opacity reset.
(b) Ballroom scene without opacity reset.

Figure 2. Comparison of the Ballroom scene from Tanks and Temples with and without opacity reset [12]. Background details are lost when opacity reset is executed, and image quality further degrades over the training process.

trim, which assures that each point is observed by multiple cameras and this is not guaranteed in sparse-view settings. Therefore, we deactivate this trimming for our method. Another parameter that requires adjustment is the opacity reset interval. When opacity reset happens, fine details in the background will be lost and artifacts appear, as can be seen in Fig. 2. The details in Fig. 2a at the back wall are completely lost and artifacts in the window frame become visible. By continuing the training process even further, the artifacts’ strength increases, and they become even more prominent. When deactivating opacity reset, the background details are retained and the artifacts vanish without sacrificing the overall quality. This can also be seen in Fig. 2b. The improvement is also reflected in the PSNR (Peak Signal-to-Noise Ratio), which increases from 22.76 to 23.73. With these few settings, it is already possible to run the PGSR framework with acceptable results. For improved performance, we deactivate the splitting strategy as it is not needed for our dense point cloud initialization. The point cloud is already very detailed and this setting does not improve the final results (cf. Tab. 1).

3.3. Dense Initialization

Sparse-view settings pose a fundamental challenge for standard SfM frameworks like COLMAP [21, 22], where limited image overlap can lead registration to fail. Furthermore, the resulting sparse point clouds serve as a poor initialization for 3DGS, complicating the optimization of Gaussian primitives and compromising geometric fidelity. To mitigate this, we leverage a pre-trained feed-forward network to predict both depth and camera parameters. This strategy provides the dense geometric initialization and accurate poses required for high-quality sparse-view reconstruction. Figure 3a illustrates the point cloud generated by the feed-forward model π^3 [25], while Fig. 3b depicts the result from COLMAP [21]. Both methods use the same 24 input views from the “bicycle” scene of the MipNeRF360 dataset [3], rendered here from an identical viewpoint. The difference in density is significant: The COLMAP reconstruction contains only 1,028 points, whereas π^3 yields 1,013,106 points. Note that the π^3 output was filtered using the default confidence threshold of 20%.



(a) Point cloud inferred with π^3 .



(b) Point cloud created with COLMAP.

Figure 3. Comparison between π^3 point cloud and COLMAP point cloud, of the bike scene from MipNeRF360 Dataset with 24 training images [3, 21, 25].

3.4. Depth Supervision

From π^3 , we obtain the per view point clouds which can be used as a depth map. For depth regularization, we evaluated different losses.

Standard L1 and L2 losses often cause the model to overfit to the limited fidelity of the inferred depth maps. We also evaluated the Global-Local Depth Normalization from *DNGaussian* [14] but found it unnecessary given the inherent scale consistency of our predictions. Instead, we utilize a Pearson correlation loss, which has demonstrated superior performance. This approach enforces structural consistency while enabling the recovery of high-frequency details that are missing from the initial depth estimation.

In addition to the default Pearson correlation loss, we also integrated the confidence given by π^3 . As a result, the final depth can be modeled even more accurately by assigning low weights to uncertain regions. Our newly created confidence-aware depth loss, $\mathcal{L}_{pearson}$, is defined as:

$$\mu_p = \frac{\sum_{i=1}^N C_i D_i^p}{\sum_{i=1}^N C_i}, \quad \mu_t = \frac{\sum_{i=1}^N C_i D_i^t}{\sum_{i=1}^N C_i}, \quad (12)$$

$$\bar{D}_p = D_p - \mu_p, \quad \bar{D}_t = D_t - \mu_t, \quad (13)$$

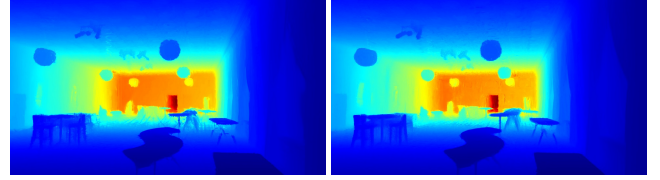
$$P_{conf} = \frac{\sum_{i=1}^N C_i \bar{D}_i^p \bar{D}_i^t}{\sqrt{\left(\sum_{i=1}^N C_i (\bar{D}_i^p)^2\right) \left(\sum_{i=1}^N C_i (\bar{D}_i^t)^2\right)}}, \quad (14)$$

$$\mathcal{L}_{pearson} = 1 - P_{conf}, \quad (15)$$

N is the number of pixels, D_i^p is the predicted depth of the i -th pixel, C_i the confidence of the i -th pixel and D_i^t is the ground truth of the i -th pixel, which is the depth estimated by π^3 , and P_{conf} is the confidence-aware Pearson correlation. The resulting rendered depth after 7,000 iterations with the help of confidence-aware Pearson correlation can be seen in Fig. 4.

3.5. Normal Supervision

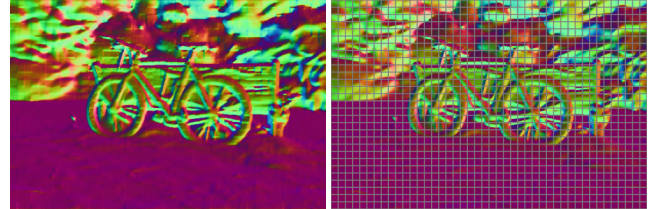
Surface Normals can be computed with the help of depth maps by calculating the pixel-wise partial derivatives $\frac{\partial z}{\partial x}$ and $\frac{\partial z}{\partial y}$, where x and y are the pixel coordinates and z is the depth value, either rendered or estimated by π^3 .



(a) Confidence-aware Pearson loss.

(b) Pearson loss.

Figure 4. Depth rendering of the Ballroom scene from the Tanks and Temples dataset, comparing the confidence-aware Pearson loss with the standard Pearson loss [12]. The confidence-aware loss leverages uncertainty estimates to enhance detail, particularly in the background, and also improves performance with low-resolution depth estimates.



(a) Default normal map with artifacts.

(b) Masked normal map.

Figure 5. The Normal map generated from the depth map using partial derivatives, which introduces grid artifacts, and the masked normal map, which removes grid artifacts introduced by π^3 architecture [25].

Because π^3 processes each image in patches of 14×14 pixels, the gradient is not continuous between adjacent patches, leading to grid-like artifacts, as can be seen in Fig. 5a. To alleviate this problem, we add a mask to ignore these discontinuous regions during loss computation. The mask is computed by creating a grid with 14×14 pixel cells, masking the 1-pixel-wide inner border of each cell. Therefore, the Gaussians are not regularized in these border regions, and the grid artifacts do not appear in the scene representation. The masked normal map can be seen in Fig. 5b. As supervision, we simply use the L1 loss between the rendered and ground-truth normal map defined as:

$$\mathcal{L}_{normal} = \frac{1}{N} \sum_{i=1}^N \|N_i^t - N_i^p\|_1, \quad (16)$$

where N is the number of pixels, N_i^t is the ground-truth normal at pixel i and N_i^p is the predicted normal at pixel i .

3.6. Depth Warping

To improve generalization of our model further, we include pseudo-views which are generated with the help of depth warping. This is achieved by projecting the image pixels from one camera into 3D space, and then reprojecting the 3D points into the 2D image plane of a target camera. For accurate results, we only project pixels with high confidence and mask out the rest, including unseen regions. To generate high-quality pseudo-cameras, we use circle interpolation with the camera parameters as input. A circle can be defined by three points, so we use



Figure 6. The two Figures show two reprojection examples with the applied mask for the Barn scene of the Tanks and Temples dataset [12].

the two nearest cameras to the target camera for pseudo-view generation. The positions of the three cameras define our circle. Now then interpolate by a certain amount between each pair of neighbouring views, which results in two additional views per camera. We can generate an arbitrary number of pseudo-views by adjusting the interpolation step size. However, in our experiments, two pseudo-views between each pair yielded the best results. The nearest cameras are already computed by PGSR, therefore we can reuse them. A few examples of these generated pseudo-views can be seen in Fig. 6. These pseudo-views are then used throughout training for additional supervision with the help of SSIM and L1 loss, but with a weight set to 0.1.

4. Evaluation

For testing strategy, we adhere to previous state-of-the-art models to ensure comparability. The datasets used for the evaluation are Tanks and Temples [12], MipNeRF360 [3], LLFF [15] and DTU [1].

Implementation Details. The Tanks and Temples dataset covers real-world indoor and outdoor scenes, but we only use a subset of 8 scenes, as done by other sparse-view models like *Intern-GS* and *InstantSplat*. We focus on the 3-view setting and therefore use the same train/test split. This means the testing set includes 12 images uniformly sampled without the first and last frame and the remaining set is the training set where we again uniformly sampled the 3 views [31]. For Tanks and Temples, no downsampling is applied.

The MipNeRF360 dataset contains real-world 360° indoor and outdoor scenes. For this dataset, two different approaches are used. One for the 3-view setting as defined by *Gaussian Scenes* [19] and one for the 12-view setting as defined by *SparseGS* [28]. For both settings, the 4x downsampled images are used, to adhere to the evaluation strategies of state-of-the-art models. For the 3-view setting, we use every 8th image as testing set and uniformly sample the 3 training views. For the 12-view setting, we use the split dataset provided by *SparseGS* [28]. The 12-view setting uses only 6 of the 9 scenes contained in the MipNeRF360 dataset, whereas the 3-view setting uses all 9 scenes.

The LLFF dataset contains real-world forward-facing images. For this dataset, we used the same evaluation

strategy as defined by *DNGaussian*. A downsampling rate of 8 is used, and we adhere to the train/test split of the 3-view setting of *DNGaussian* [14].

Lastly, we also evaluated on the DTU dataset, which contains highly calibrated lab captures of object centric scenes. This dataset also provides bit masks to separate the background and real camera poses. We used our own inferred camera poses. We again used the testing strategy defined by *DNGaussian*. This time we used 4x downsampled images and the same train/test split of the 3-view setting of *DNGaussian* [14]. Similar to *DNGaussian* and other comparable methods, we applied the provided separation masks for the evaluation.

We use the exact same settings for all evaluations. π^3 [25] automatically downsample the images to a certain pixel size, therefore we counteract the downsampling by rescaling the cameras to the full size. To make a fair comparison, we only project the training views to 3D space. The testing views are only used to get initial camera positions. We train for 7000 iterations, with depth loss, normal loss as well as pseudo views. The pseudo views are generated with a confidence threshold of 20%. This means that we mask out the projected pixel with confidence under 20%. Splitting of Gaussians is deactivated. We evaluate our model in terms of PSNR, SSIM and LPIPS.

4.1. Quantitative Evaluation

Tables 3 and 6 show the comparison between *Intern-GS* [27], *InstantSplat* [31], *SparseGS* [28], *DNGaussian* [14], *FSGS* [33], 3DGS [11] and Our method. On DTU and Tanks and Temples, our model can reconstruct the scene accurately, with good Gaussian surface alignment and without smoothing out high-frequency textures. On LLFF our model achieves slightly lower scores, because of missing information in unseen regions, as our model optimizes only on seen regions and known information. An example of this unseen region is illustrated in Fig. 7.

Tab. 4 shows the comparison between Gaussian Scenes, MASt3R Initialization, FSGS and Our method in the 3-view setting on MipNeRF360 [19, 33]. Our model achieves the lowest LPIPS score and second highest PSNR and SSIM. Compared to FSGS our model does not rely on accurate camera poses from traditional SfM.

Tab. 5 shows the comparison between 3DGS, *DNGaussian*, *SparseGS* and Our method in 12-view setting on MipNeRF360 [3]. Our model achieves the highest results with very coherent and view-consistent final scene, as our model improves the Gaussian surface alignment significantly. A comparison can be seen in Fig. 8.

To validate the accuracy of our camera pose estimates, we evaluate the Absolute Trajectory Error (ATE) on the Tank and Temples dataset. Our pose estimator, π^3 , achieves a mean ATE of 0.0293 and a root mean squared error (RMSE) of 0.0325, demonstrating that it produces accurate camera poses suitable for fair comparison of photo-

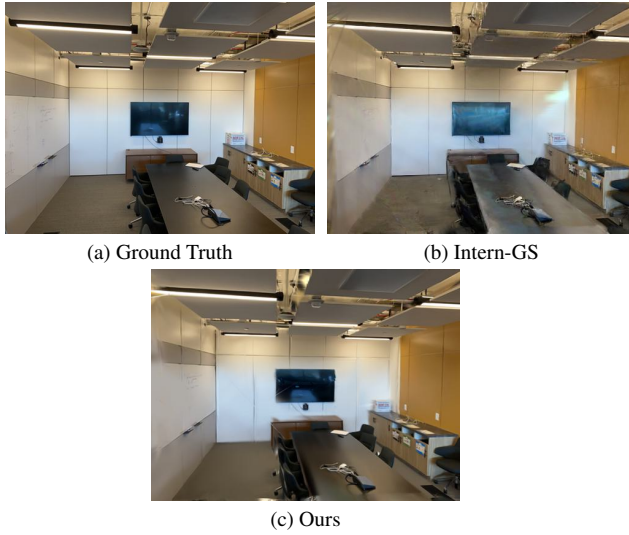


Figure 7. The Figures show a comparison between Intern-GS [27], Ours and the Ground Truth. Our model has very accurate reflections and fewer artifacts, nevertheless our model can not correctly reconstruct the unseen region at the ceiling.



Figure 8. The Figures show a comparison between SparseGS [28] and our method. Our model reconstructs the background and ground more accurately, and additionally decreases artifacts.

metric metrics in 3D Gaussian splatting.

4.2. Ablation

We evaluate the impact of each individual optimization on our final result. The evaluation is conducted using the Barn scene from the Tanks and Temples dataset. It is evident that all of our optimizations improve the result even further. Dense point cloud initialization with the help of π^3 significantly improves the result by also reducing the time required for SfM. Our custom depth loss improves the score by allowing low confidence depth regions to optimize more freely. Normal regularization encourages the Gaussians' normals to match the ground-truth geometry. Depth warping improves the results by adding more views, which helps the model generalize better and avoid overfitting to the training views. Our full model achieves a PSNR of 22.15 on the Barn scene. We also evaluated the effect of enabling splitting of Gaussians in our model. This setting results in a slight decrease in performance and was therefore deactivated. These results can be seen in

Tab. 1.

Method	PSNR
Original 3DGS	17.53
PGSR	18.05
π^3 (dense) initialization	19.66
+ Depth Regularization	20.72
+ Normal Regularization	21.56
+ Depth Warping (Full Model)	22.15
+ Splitting Densification	21.97

Table 1. Ablation study of the regularization techniques introduced in our model on the Barn scene of Tanks and Temples. Additionally, we evaluated the impact of splitting Gaussians during densification.

In addition, we evaluate the impact of using PGSR compared to standard 3DGS for our sparse view setting (3-views). Table 2 shows that the planar depth created by PGSR helps significantly to place the Gaussians more accurately. Additionally, the losses introduced by PGSR help to improve the rendering results further. Our model remains stable even after increased training iterations and continues to show improved novel view synthesis results. A visual comparison between 3DGS and PGSR with different number of iterations can be seen in Fig. 9.

Framework	Iteration	Tanks and Temples			MipNeRF360		
		PSNR \uparrow	SSIM \uparrow	LPIPS \downarrow	PSNR \uparrow	SSIM \uparrow	LPIPS \downarrow
PGSR [4]	7000	19.99	0.503	0.355	23.36	0.791	0.156
3DGS [11]	7000	18.00	0.426	0.449	23.07	0.773	0.172
PGSR [4]	15000	20.19	0.517	0.343	23.41	0.795	0.169
3DGS [11]	15000	17.04	0.391	0.465	20.94	0.719	0.244

Table 2. Ablation study on the use of PGSR as base framework compared to 3DGS. The additional multi-view and single-view losses introduced by PGSR are activated after iteration 7000. This comparison shows that the PGSR depth rendering captures the underlying surface geometry more accurately by also reducing floaters significantly. With the help of PGSR we achieve view-consistent surfaces and reduce overfitting significantly.

Method	PSNR \uparrow	SSIM \uparrow	LPIPS \downarrow
3DGS [11]	15.36	0.572	0.379
DNGaussian [14]	20.69	0.721	0.277
SparseGS [28]	21.20	0.717	0.231
InstantSplat [31]	22.20	0.743	0.199
FSGS [33]	22.31	0.693	0.197
Intern-GS [27]	22.67	0.736	0.191
Ours	22.87	0.764	0.189

Table 3. Evaluation on Tanks and Temples dataset with 3-view setting. Our model does not oversmooth high-frequency textures and accurately aligns the Gaussians with the underlying surface geometry.

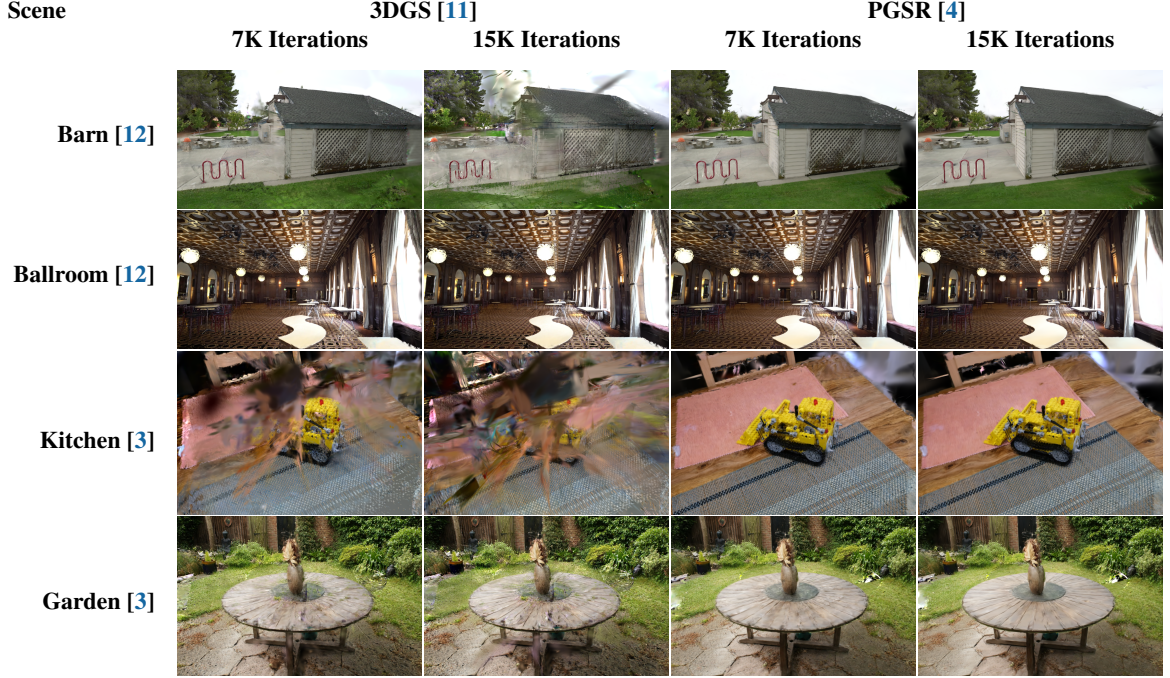


Figure 9. Visual comparison between 3DGS and PGSR with different Iterations. The planar depth from PGSR helps significantly to remove floaters and align the Gaussians accurately to the ground-truth geometry.

Method	PSNR \uparrow	SSIM \uparrow	LPIPS \downarrow
MAS3R Initialization [19]	12.59	0.231	0.593
Gaussian Scenes [19]	13.81	0.265	0.547
FSGS [33]	14.17	0.318	0.578
Ours	14.14	0.310	0.523

Table 4. Evaluation on MipNeRF360 dataset with 3-view setting. Our model reconstructs seen regions accurately, but can not introduce geometry in unseen regions.

Method	PSNR \uparrow	SSIM \uparrow	LPIPS \downarrow
3DGS [11]	17.49	0.490	0.431
DNGaussian [14]	16.28	0.432	0.549
SparseGS [28]	19.37	0.577	0.398
Ours	19.54	0.492	0.362

Table 5. Evaluation on MipNeRF360 dataset with 12-view setting. Our model can reconstruct the scenes with highly accurate surface alignment. The ground is view-consistent, and fewer floating artifacts compared to SparseGS [28].

5. Conclusion and Limitations

Our model shows strong performance under sparse-view constraints, specifically when handling between 3 and 12 views. The model demonstrates the importance of accurate dense point cloud initialization. We introduce a modified depth loss that enables correct scene generalization by reducing depth ambiguities without introducing artifacts in low confidence regions. In addition, we introduce normal and depth warping loss terms that improve alignment with the ground-truth surface geometry. Finally, we

Method	LLFF			DTU		
	PSNR \uparrow	SSIM \uparrow	LPIPS \downarrow	PSNR \uparrow	SSIM \uparrow	LPIPS \downarrow
3DGS [11]	15.52	0.408	0.405	10.99	0.585	0.313
DNGaussian [14]	19.12	0.591	0.294	18.91	0.790	0.176
SparseGS [28]	19.86	0.668	0.322	18.89	0.834	0.178
InstantSplat [31]	17.67	0.603	0.379	17.55	0.634	0.212
FSGS [33]	20.31	0.652	0.288	19.54	0.732	0.199
Intern-GS [27]	20.49	0.693	0.212	20.34	0.851	0.163
Ours	19.92	0.664	0.254	23.52	0.815	0.145

Table 6. Evaluation on LLFF and DTU dataset with 3-view setting. Following previous work, for evaluation on DTU the background masks are applied. Our model is able to reconstruct fine-grained textures accurately, but it underperforms in unobserved regions compared to methods that generate content for unseen regions.

relax certain assumptions from PGSR to allow robust optimization in sparse-view settings.

Our model faces limitations when dealing with large datasets, as processing many input views with π^3 consumes a large amount of GPU memory, which is infeasible on consumer hardware. Additional limitations come from inaccurate depth estimations in specific scenes, such as the leaves scene from the LLFF dataset [15]. Future improvements could include the joint optimization of the camera poses and the Gaussian scene, which would result in improved reconstruction quality. Furthermore, the integration of generative priors could enhance the model’s ability to maintain photometric and geometric consistency across occluded or sparse areas.

References

[1] Henrik Aanaes, Rasmus Ramsbøl Jensen, George Vogiatzis, Engin Tola, and Anders BJORHOLM Dahl. Large-Scale Data for Multiple-View Stereopsis. *IJCV*, pages 1–16, 2016. 6

[2] Allison H. Baker, Alexander Pinard, and Dorit M. Hämmerling. On a Structural Similarity Index Approach for Floating-Point Data. *IEEE TVCG*, 30(9):6261–6274, 2024. 3

[3] Jonathan T. Barron, Ben Mildenhall, Dor Verbin, Pratul P. Srinivasan, and Peter Hedman. Mip-NeRF 360: Unbounded Anti-Aliased Neural Radiance Fields. In *Proc. CVPR*, pages 5470–5479, 2022. 4, 5, 6, 8

[4] Danpeng Chen, Hai Li, Weicai Ye, Yifan Wang, Weijian Xie, Shangjin Zhai, Nan Wang, Haomin Liu, Hujun Bao, and Guofeng Zhang. PGSR: Planar-Based Gaussian Splatting for Efficient and High-Fidelity Surface Reconstruction. *IEEE TVCG*, 2024. 2, 3, 4, 7, 8

[5] Kai Cheng, Xiaoxiao Long, Kaizhi Yang, Yao Yao, Wei Yin, Yuexin Ma, Wenping Wang, and Xuejin Chen. GaussianPro: 3D Gaussian Splatting with Progressive Propagation. In *Proceedings of the 41st International Conference on Machine Learning (ICML 2024)*, 2024. 4

[6] Jaeyoung Chung, Jeongtaek Oh, and Kyoung Mu Lee. Depth-Regularized Optimization for 3D Gaussian Splatting in Few-Shot Images. In *Proc. CVPRW*, pages 811–820, 2024. 2

[7] Bardienus Pieter Duisterhof, Lojze Zust, Philippe Weinzaepfel, Vincent Leroy, Yohann Cabon, and Jerome Revaud. MAST3R-SfM: a Fully-Integrated Solution for Unconstrained Structure-from-Motion. In *Proc. 3DV*, 2025. 2

[8] Yang Fu, Sifei Liu, Amey Kulkarni, Jan Kautz, Alexei A. Efros, and Xiaolong Wang. COLMAP-Free 3D Gaussian Splatting. In *Proc. CVPR*, pages 20796–20805, 2024. 2

[9] Tao Hu, Shu Liu, Yilun Chen, Tiancheng Shen, and Jiaya Jia. EfficientNeRF: Efficient Neural Radiance Fields. In *Proc. CVPR*, pages 12902–12911, 2022. 2

[10] Michael Kazhdan, Matthew Bolitho, and Hugues Hoppe. Poisson surface reconstruction. In *Proc. SGP*, 2006. 2

[11] Bernhard Kerbl, Georgios Kopanas, Thomas Leimkuehler, and George Drettakis. 3D Gaussian Splatting for Real-Time Radiance Field Rendering. *ACM TOG*, 2023. 1, 2, 3, 6, 7, 8

[12] Arno Knapitsch, Jaesik Park, Qian-Yi Zhou, and Vladlen Koltun. Tanks and Temples: Benchmarking Large-Scale Scene Reconstruction. *ACM TOG*, 36(4), 2017. 4, 5, 6, 8

[13] Raja Kumar and Vanshika Vats. Few-Shot Novel View Synthesis Using Depth Aware 3D Gaussian Splatting. In *ECCV 2024 Workshops*, pages 1–13, Cham, 2025. Springer Nature Switzerland. 2

[14] Jiahe Li, Jiawei Zhang, Xiao Bai, Jin Zheng, Xin Ning, Jun Zhou, and Lin Gu. DNGaussian: Optimizing Sparse-View 3D Gaussian Radiance Fields with Global-Local Depth Normalization. In *Proc. CVPR*, pages 20775–20785, 2024. 2, 5, 6, 7, 8

[15] Ben Mildenhall, Pratul P. Srinivasan, Rodrigo Ortiz-Cayon, Nima Khademi Kalantari, Ravi Ramamoorthi, Ren Ng, and Abhishek Kar. Local Light Field Fusion: Practical View Synthesis with Prescriptive Sampling Guidelines. *ACM TOG*, 2019. 6, 8

[16] Ben Mildenhall, Pratul P. Srinivasan, Matthew Tancik, Jonathan T. Barron, Ravi Ramamoorthi, and Ren Ng. NeRF: Representing Scenes as Neural Radiance Fields for View Synthesis. *Communications of the ACM*, 65(1): 99–106, 2021. 1, 2

[17] Thomas Müller, Alex Evans, Christoph Schied, and Alexander Keller. Instant Neural Graphics Primitives with a Multiresolution Hash Encoding. *ACM TOG*, 41(4): 102:1–102:15, 2022. 2

[18] Hyunwoo Park, Gun Ryu, and Wonjun Kim. DropGaussian: Structural Regularization for Sparse-view Gaussian Splatting. In *Proc. CVPR*, pages 21600–21609, 2025. 2

[19] Soumava Paul, Prakhar Kaushik, and Alan Yuille. Gaussian Scenes: Pose-Free Sparse-View Scene Reconstruction using Depth-Enhanced Diffusion Priors. *arXiv preprint arXiv:2411.15966*, 2024. 3, 6, 8

[20] Fabio Remondino, Ali Karami, Ziyang Yan, Gabriele Mazzacca, Simone Rigon, and Rongjun Qin. A Critical Analysis of NeRF-Based 3D Reconstruction. *Remote Sensing*, 15(14), 2023. 2

[21] Johannes Lutz Schönberger and Jan-Michael Frahm. Structure-from-Motion Revisited. In *Proc. CVPR*, 2016. 4, 5

[22] Johannes Lutz Schönberger, Enliang Zheng, Marc Pollefeys, and Jan-Michael Frahm. Pixelwise View Selection for Unstructured Multi-View Stereo. In *Proc. ECCV*, 2016. 4

[23] Hamid Taheri and Zhao Chun Xia. SLAM; definition and evolution. *Engineering Applications of Artificial Intelligence*, 97:104032, 2021. 1

[24] Shuzhe Wang, Vincent Leroy, Yohann Cabon, Boris Chidlovskii, and Jerome Revaud. DUSt3R: Geometric 3D Vision Made Easy. In *Proc. CVPR*, 2024. 2

[25] Yifan Wang, Jianjun Zhou, Haoyi Zhu, Wenzheng Chang, Yang Zhou, Zizun Li, Junyi Chen, Jiangmiao Pang, Chunhua Shen, and Tong He. π^3 : Scalable Permutation-Equivariant Visual Geometry Learning. *arXiv preprint arXiv:2507.13347*, 2025. 4, 5, 6

[26] Sibo Wu, Congrong Xu, Binbin Huang, Andreas Geiger, and Anpei Chen. Genfusion: Closing the loop between reconstruction and generation via videos. In *Proc. CVPR*, pages 6078–6088, 2025. 3

[27] Sun Xiangyu, Chen Runnan, Gong Mingming, Xu Dong, and Liu Tongliang. Intern-GS: Vision Model Guided Sparse-View 3D Gaussian Splatting. *arXiv preprint arXiv:2505.20729*, 2025. 2, 3, 6, 7, 8

[28] Haolin Xiong, Sairisheek Muttukuru, Hanyuan Xiao, Rishi Upadhyay, Pradyumna Chari, Yajie Zhao, and Achuta Kadambi. SparseGS: Sparse View Synthesis Using 3D Gaussian Splatting. In *Proc. 3DV*, pages 1032–1041, 2025. 2, 3, 6, 7, 8

[29] Yexing Xu, Longguang Wang, Minglin Chen, Sheng Ao, Li Li, and Yulan Guo. DropoutGS: Dropping Out Gaussians for Better Sparse-view Rendering. In *Proc. CVPR*, pages 701–710, 2025. 2

[30] Alex Yu, Ruiyang Li, Matthew Tancik, Hao Li, Ren Ng, and Angjoo Kanazawa. PlenOctrees for Real-Time Rendering of Neural Radiance Fields. In *Proc. ICCV*, pages 5752–5761, 2021. 2

[31] Fan Zhiwen, Wen Kairun, Cong Wenyan, Wang Kevin, Zhang Jian, Ding Xinghao, Xu Danfei, Ivanovic Boris,

Pavone Marco, Pavlakos Georgios, Wang Zhangyang, and Wang Yue. InstantSplat: Sparse-view Gaussian Splatting in Seconds. *arXiv preprint arXiv:2403.20309*, 2024. [2](#), [6](#), [7](#), [8](#)

[32] Yiming Zhou, Zixuan Zeng, Andi Chen, Xiaofan Zhou, Haowei Ni, Shiyao Zhang, Panfeng Li, Liangxi Liu, Mengyao Zheng, and Xupeng Chen. Evaluating Modern Approaches in 3D Scene Reconstruction: NeRF vs Gaussian-Based Methods. In *Proc. DOCS*, pages 926–931, 2024. [1](#)

[33] Zehao Zhu, Zhiwen Fan, Yifan Jiang, and Zhangyang Wang. Fsgs: Real-time few-shot view synthesis using gaussian splatting. In *Proc. ECCV*, page 145–163, Berlin, Heidelberg, 2024. Springer-Verlag. [2](#), [6](#), [7](#), [8](#)

[34] Onur Özyeşil, Vladislav Voroninski, Ronen Basri, and Amit Singer. A Survey of Structure from Motion. *Acta Numerica*, 26:305–364, 2017. [2](#)